Electronic Supplementary Material (ESI) for Physical Chemistry Chemical Physics.

Supporting Information

Microfluidic Out-of-Equilibrium Control of Molecular Nanotubes

Björn Kriete[1], Carolien Feenstra[1], and Maxim S. Pshenichnikov[1,*]

[1]University of Groningen, Zernike Institute for Advanced Materials, Nijenborgh 4, 9747 AG Groningen, the Netherlands

[*]Corresponding author: M.S.Pchenitchnikov@rug.nl

Table of Contents

1. Reduced Linear Dichroism

Linear dichroism spectra of double-walled nanotubes and isolated inner tubes were obtained by measuring absorption spectra with the excitation light polarized parallel and perpendicular with respect to the flow direction of the sample in the microfluidic channel. Light of a white light source (Ocean Optics, HL-2000) was collimated, sent through a linear polarizer (Thorlabs, LPVISE100-A) and focused into the microfluidic channel containing the nanotubes sample solution by a $f = 6$ cm lens (Supplementary Figure 1). An adjustable aperture was used to reduce the focal spot size at the sample position to about ~400 µm (diameter). Next, the transmitted light was coupled into a multi-mode optical fiber and detected by a spectrometer (Ocean Optics, USB4000) with a spectral resolution of ~1.5 nm (FWHM). Measurements for parallel and perpendicular polarization were averaged for 50 s and carried out successively by turning the polarizer by 90° between the measurements. The polarization dependent absorption spectra, i.e., $A_{||}$ and $A_{\perp}$ for parallel and perpendicular polarization, respectively, were calculated against a reference recorded for pure water.

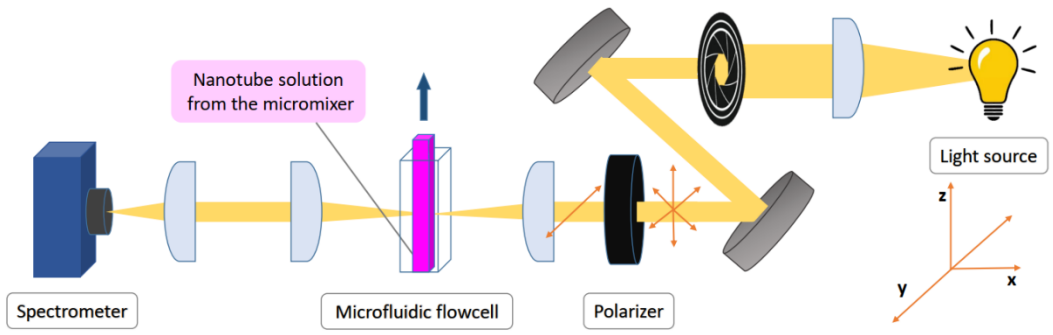

Supplementary Figure 1. Schematic of the experimental setup for polarized absorption measurement for linear dichroism of isolated inner tubes. The flow direction is indicated by the blue arrow. In the schematic, the polarizer sets the light polarization parallel to the flow direction of the sample (y-axis).

The reduced linear dichroism (LD_r) was then determined as the difference of parallel and perpendicular polarized spectra and normalized by the isotropic absorption (A_{iso}):

$$LD_r = \frac{A_{||} - A_{\perp}}{A_{iso}} = \frac{A_{||} - A_{\perp}}{\frac{1}{3}(A_{||} + 2A_{\perp})}. \quad (1.1)$$

Compared to conventional linear dichroism (simply defined as the difference $A_{||} - A_{\perp}$) the reduced quantity LD_r offers the advantage that the signal amplitude is insensitive to measurement

parameters such as the molar concentration of the sample or the thickness of the cuvette. Hence, it can be interpreted as a pure measure of the alignment (or polarization) of the sample.

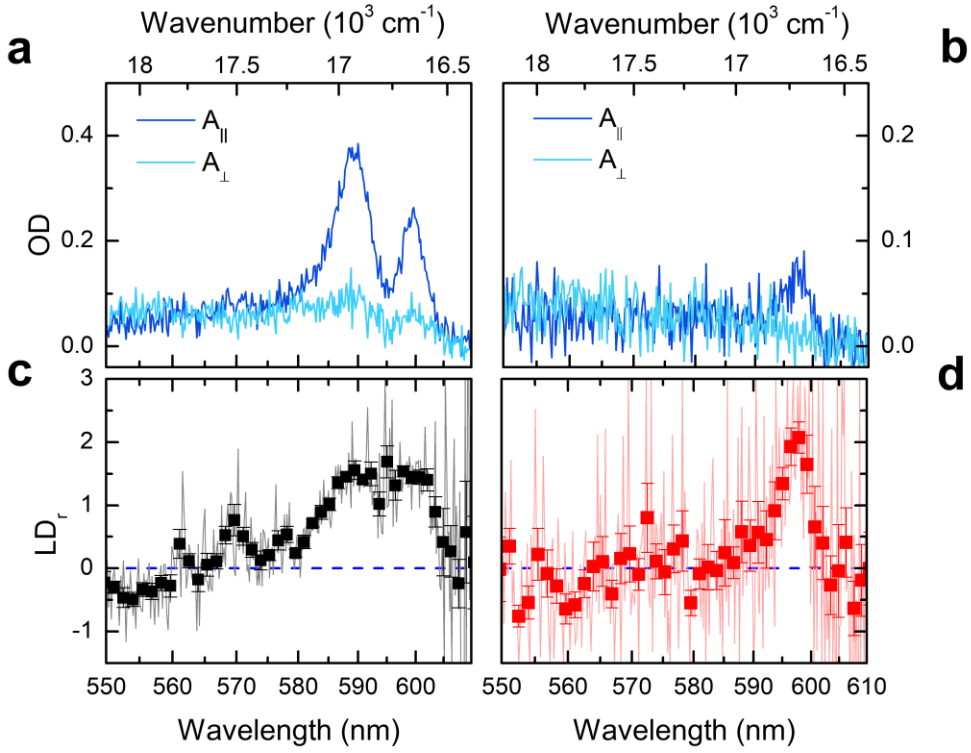

Supplementary Figure 2. Raw absorption spectra for (a) double-walled nanotubes and (b) isolated inner tubes for parallel ($A_{||}$, blue) and perpendicular ($A_{\perp}$, light blue) polarization of the excitation light. The corresponding $\mathrm{LD_r}$ spectra are shown as black and red lines in panel (c) and (d), respectively. Averaged data for seven adjacent data points along the wavelength axis are shown as dots; the same data are shown in Figure 3 in the main text. The error margins refer to the standard error of the mean. The case of isotropic absorption ($\mathrm{LD_r} = 0$) is shown by a dashed horizontal line.

The raw absorption spectra for double-walled nanotubes and isolated inner tubes for both polarizations (i.e., $A_{||}$ and $A_{\perp}$ prior to computing the reduced linear dichroism) are shown in Supplementary Figure 2a and b, respectively. The reduced linear dichroism spectra are shown in Supplementary Figure 2c and d. To improve the signal-to-noise ratio, seven adjacent data points along the wavelength axis were binned and averaged; these are also overlaid in with the raw data Supplementary Figure 2c and d. This operation does not compromise the spectral resolution ($\sim$1.5 nm; FWHM), as it is significantly larger than the optical resolution (0.2 nm pixel^{-1}) of the spectrometer. The signal to noise ratio in our LD measurements is mainly limited by the thin channel thickness (50 µm) and, thus, low light absorption. That means the signal-to-noise ratio

could potentially be improved by e.g. manufacturing flowcells with a thicker channel. Here, we used identical conditions for all experiments to ensure their cross-comparability.

A positive LD_r value means a transition is parallel with respect to orientation (or symmetry) axis of the sample, because $A_{||} > A_{\perp}$. Likewise, a negative LD_r value means a transition is polarized perpendicular ($A_{||} < A_{\perp}$). The maximum (minimum) LD_r amplitudes are 3 (-1.5) for perfectly parallel (perpendicular) polarized transitions. Misalignment of the nanotubes' orientation along the flow direction as well as spectral overlap of transitions with different orientation of transient dipole moments lead to deviations from these ideal cases and, thus, lower LD_r values. In addition to that, shear effects due to the channel walls leading to a lower local flow rate may also affect the attainable maximum LD_r amplitude. As light propagates through the channel, this effect is intrinsically averaged in our measurements with contributions from both slowly and quickly flowing sample solution close to the channel edge and center, respectively.

2. Experimental Apparatus for Time-Resolved PL Experiments

Time-resolved PL experiments were carried out on a streak camera (Hamamatsu, model C5680) based setup coupled to an inverted microscope (Supplementary Figure 3). Excitation pulses of the desired wavelength were obtained by focusing the output of a Ti:Sapphire oscillator (Coherent Mira, repetition rate 80 MHz, 150 fs) into a hollow fiber (Newport SCG-800) and subsequently selecting a narrow spectral portion of the generated white light with a 550 ± 5 nm bandpass filter. A combination of an achromatic $\lambda/2$-waveplate (Thorlabs), a polarizer and neutral density filters was used to adjust the average power of the excitation light at the sample plane. A longpass dichroic mirror (DM, transmission edge at 567 nm) directed the excitation beam towards the microfluidic flow-cell, where an objective (Melles Griot, $10\times$ magnification, NA $= 0.26$) focused the excitation beam into the microfluidic channel. The same objective was used to collect and collimate the PL signal emitted by the sample, which then was transmitted by the DM to the backport of the microscope. Residual excitation light that leaked through the DM was blocked by a bandpass filter (605 ± 90 nm) and a 570 nm longpass filter. The PL signal was later corrected for the transmission characteristics of this filter arrangement. The polarization of the excitation laser was set parallel to the flow direction of the sample.

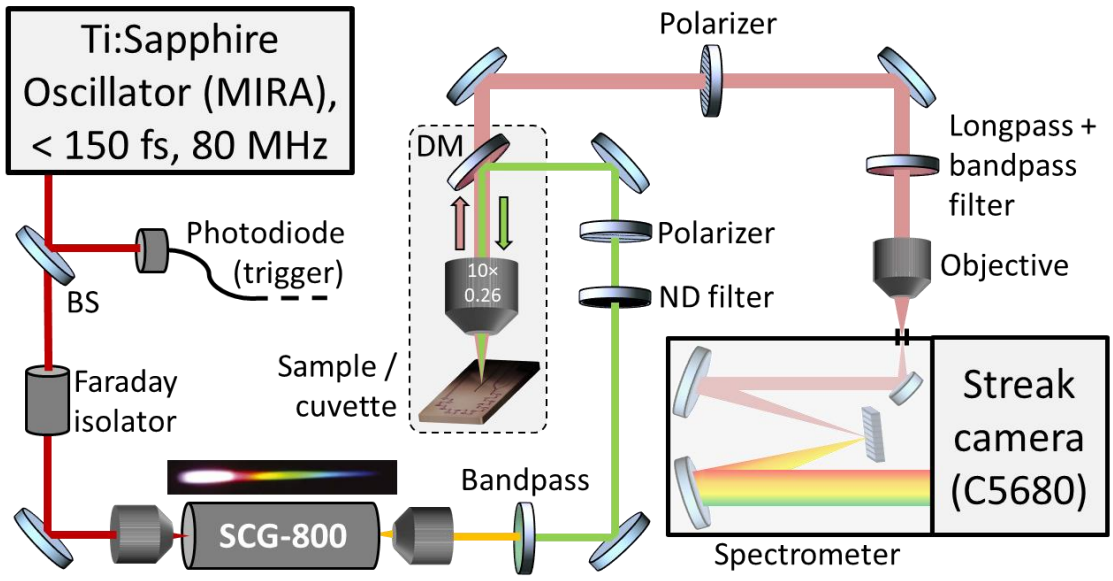

Supplementary Figure 3. Schematic of the experimental apparatus for time-resolved photoluminescence spectroscopy coupled to an inverted microscope (dashed box). The used acronyms are: BS: beam-splitter, DM: dichroic mirror. SCG-800 (Newport): photonic crystal fiber for supercontinuum (white light) generation.

Next, we determined intensity distribution of the excitation spot in EEA PL experiments using two methods: (i) via direct imaging of the excitation spot and (ii) by scanning a photoluminescent nanobead through the excitation spot and recording a sequence of images.

For direct imaging, the excitation light was focused onto a spin-coated, thin film (thickness ~600 nm) of diluted sulforhodamine 101 (SR101) dye embedded in a PMMA matrix by an NA $=$ 0.26 objective (Melles Griot, 10 × magnification). The PL was collected by the same objective and imaged with a CCD camera (Photonmetric Coolsnap HQ2) and an image magnifier (1.6 ×). The thus obtained image of the excitation spot is shown in Supplementary Figure 4.

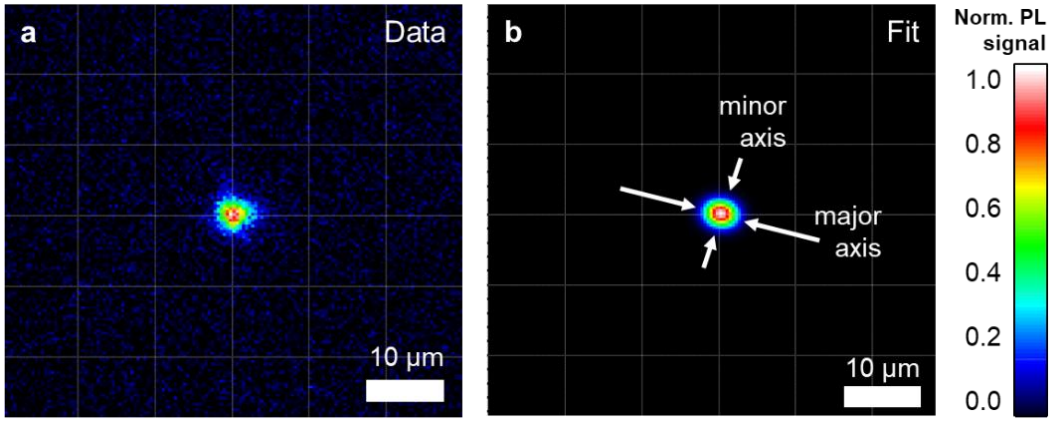

Supplementary Figure 4. (a) Image of the excitation spot. (b) Two-dimensional Gaussian fit of the excitation spot. In both panels the PL intensity was normalized to the maximum amplitude in the image and is depicted on a linear color scale between 0 and 1.

In order to extract the size of excitation spot the measured intensity pattern is fitted to a two-dimensional Gaussian function. Therefore, the coordinate frame is transformed so that the x- and y-coordinates in the image are parallel to the long (major) and short (minor) axis of the Gaussian function. Fitting then yields $\mathrm{FWHM}_{\mathrm{minor}} = 3.00 \pm 0.04$ µm and $\mathrm{FWHM} = 3.43 \pm 0.04$ µm, where error margins refer to the standard deviation of the fit. From these values the effective FWHM of the excitation spot can be determined as $\mathrm{FWHM}_{\mathrm{eff}} = \sqrt{3.0 \times 3.4}$ µm $= 3.21 \pm 0.03$ µm.

As a second way to measure the size of the excitation spot we used a photoluminescent nanobead ($Ø = 40$ nm), which allows to accurately sample the intensity distribution of the excitation spot due to its small size. In experiment, the nanobead was moved through the excitation

spot in steps of ~0.36 µm using piezo-stage and an image was recorded at each step. Integration of the PL intensity for each image and plotting it as a function of the position of the nanobead then results in a linescan of the intensity distribution of the excitation spot (Supplementary Figure 5). Fitting the experimental data to a Gaussian function yields FWHM $= 2.8 \pm 0.5$ µm, which confirms the results from direct imaging of the excitation spot.

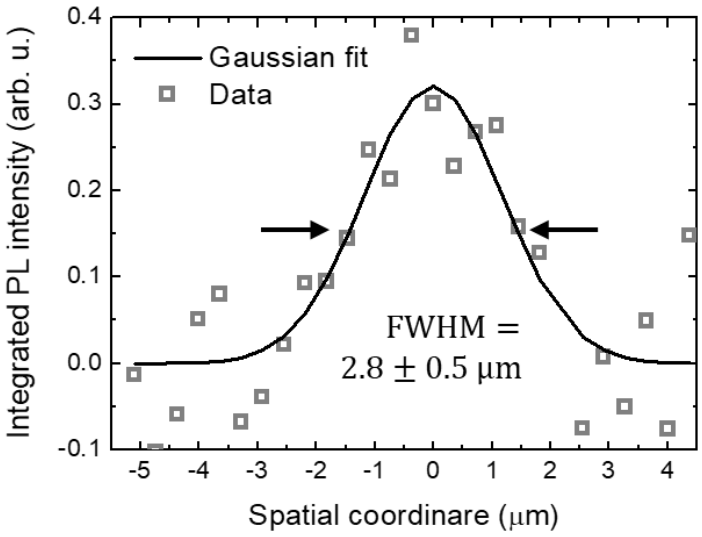

Supplementary Figure 5. Linescan of a photoluminescent nanobead through the excitation spot for EEA PL experiments. Integrated PL intensity (gray, open dots) and corresponding Gaussian fit (solid black lined) with a width of 2.8 ± 0.5 µm.

3. Photoluminescence Measurements with 530 nm Excitation

In order to prove that C8S3 monomers do not contribute to the signal measured in PL EEA experiments, we shifted the excitation wavelength to 530 nm, where C8S3 nanotubes and monomers have an isosbestic point[1]. As a result, both species are excited equally by the excitation laser. However, due to the experimental arrangement, including dichroic mirrors and spectral filters, only the tail of the monomer PL spectrum can be glimpsed at, while the main peak around ~540 nm is cut off. Supplementary Figure 6a depicts the PL spectrum of double-walled nanotubes with the two peaks for inner (~599 nm, 16690 cm^{-1}) and outer tube (~589 nm, 16980 cm^{-1}) clearly resolved. After flash-dilution, the outer peak feature vanishes and is replaced by a plateau on the blue side of the inner tube peak (Supplementary Figure 6b), which is ascribed to the emission from dissolved monomers.

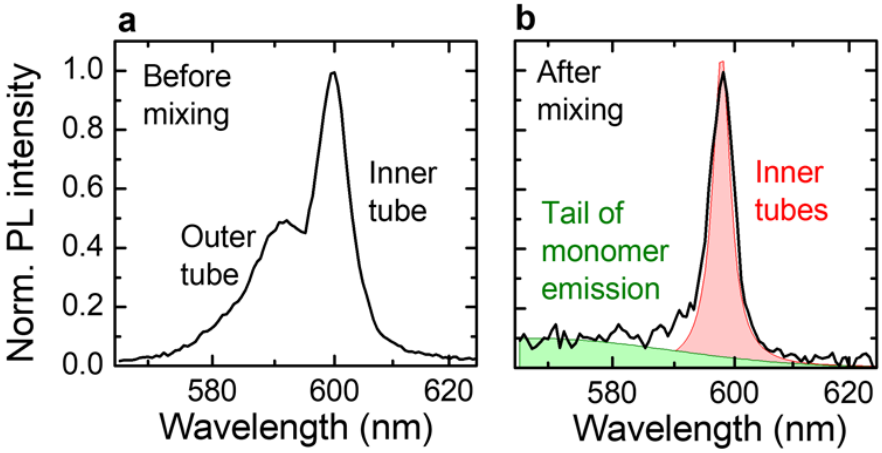

Supplementary Figure 6. PL spectra of C8S3 nanotubes (a) before and (b) after microfluidic flash-dilution following excitation at 530 nm. In panel (a) the peaks belonging to the inner (at ~600 nm) and outer tube (at ~590 nm) can clearly be distinguished. In panel (b) the experimental PL spectrum (solid black line) is fitted to the sum of a Lorentzian and a Gaussian representing the contributions of isolated inner tubes (shaded red) and monomers (shaded green), respectively.

If this assignment holds, the PL transients of the isolated inner tubes should accelerate due to EEA, whereas the monomer PL transients should remain unaffected. In order to obtain the PL transients, the PL decay maps are spectrally integrated across the plateau, i.e., between 560 – 589 nm for monomers (Supplementary Figure 7a) and between 595 – 601 nm for isolated inner tubes (Supplementary Figure 7a) for three different excitation intensities. The monomer PL transient obtained in a separate experiment is shown in comparison (black).

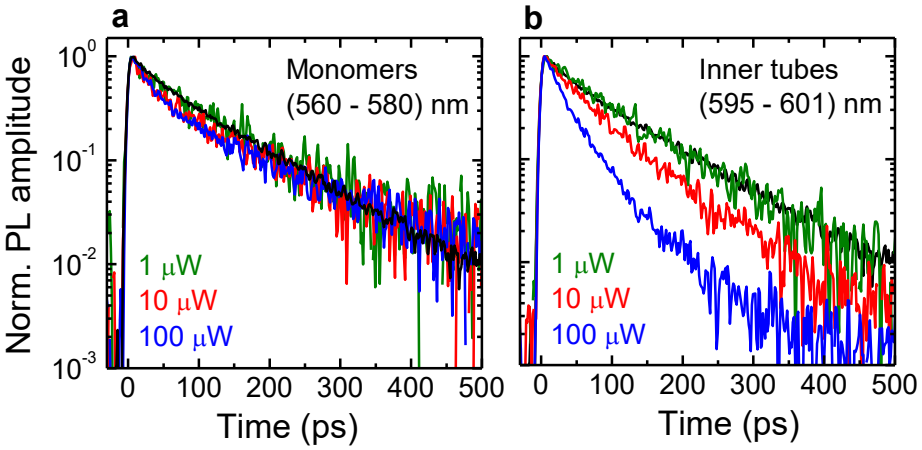

Supplementary Figure 7. Spectrally integrated PL transients for monomers in the plateau region (560 – 580 nm) and for isolated inner tubes (595 – 601 nm) at different excitation intensities. The monomer PL transient from separate measurements is shown in both panels for comparison (black).

The PL transients belonging to the isolated inner tubes clearly accelerate due to EEA. The low excitation transient (green) overlaps with the monomer transient (black), because integration of the PL signal does not separate the individual contributions from monomers and inner tubes emitting at the same wavelength. For the PL transients taken from the plateau, no indications of EEA can be found. The slight acceleration at early times is likely again due to spectral overlap of monomer and inner tube emission. However, as the PL originating from the isolated inner tubes decays faster than from the monomers, the tail (> 250 ps) of the PL transient matches the monomer decay regardless of excitation densities, which is in line with EEA measurement on diluted C8S3 monomers (ESI†, Section 9).

4. Absorption Spectra during Nanotube Recovery

In this section, we replicate the flash-dilution experiments in a conventional cuvette for two reasons: (1) to monitor the long-term evolution of the absorption spectra and, thus, the recovery of nanotubes after flash-dilution (on a timescale of several hours) that is not directly accessible with microfluidics, and (2) to estimate the molar concentration of inner tubes after flash-dilution. The latter requires a higher signal-to-noise ratio that is easier to obtain using a conventional cuvette due to the longer optical pathlength through the sample. The conditions under which flash-dilution occurs in a microfluidic cuvette (in terms of solvent composition, molar concentration, *etc.*) were replicated in a standard $1\ \mathrm{mm}$ quartz cuvette (Starna GmbH, Germany). Specifically, $150\ \mu\mathrm{l}$ of neat nanotube solution (prepared as described in the main text) were added to $210\ \mu\mathrm{l}$ of diluting agent ($1{:}\,1$ mixture of MeOH and H_2O by volume) and vigorously shaken for a few seconds to induce flash-dilution. This resulted in a molar concentration of $c = 1.11 \times 10^{-4}\ \mathrm{M}$ of the sample solution. The cuvette was then immediately transferred to the absorption spectrometer (PerkinElmer Lambda 900 UV/VIS/NIR) and a sequence of absorption spectra was recorded over a total duration of 10 minutes. Thereafter, the cuvette was stored for ~ 20 hours in the dark before another absorption spectrum was recorded.

The evolution of the absorption spectra of C8S3 nanotube solution following flash-dilution is shown in Supplementary Figure 8. In the initial spectrum (red), the peak associated with the outer tube ($\sim 589\ \mathrm{nm}$, $\sim 16980\ \mathrm{cm^{-1}}$) is absent, whereas the peak associated with the inner tube ($\sim 599\ \mathrm{nm}$, $\sim 16690\ \mathrm{cm^{-1}}$) as well as the band of excitonic transitions at higher energies (between $550\ \mathrm{nm}$ and $575\ \mathrm{nm}$) is retained. Simultaneously, a clear increase of the absorption peak of dissolved C8S3 molecules at $520\ \mathrm{nm}$ ($\sim 19230\ \mathrm{cm^{-1}}$) reveals the fate of the molecules that were formerly constituting the outer tube. As time progresses, the outer tube absorption peak gradually recovers, which is accompanied by a decrease in monomer absorption. Waiting for additional ~ 20 hours leads to a further recovery of the nanotube spectrum and decrease of monomer spectrum until the equilibrium between the two species is established. We note that compared to the initial nanotube solution, the equilibrium point between monomers and nanotubes has shifted in favor of the monomers due to the increased MeOH content of the sample. Specifically, the final MeOH content amounts to $28\ \mathrm{wt\%}$ (as compared to $11\ \mathrm{wt\%}$ initially), which is still well below the threshold for complete disintegration of the nanotubes at $39\ \mathrm{wt\%}$ reported by von Berlepsch *et*

al.[1] In the same study, the authors have shown that no other supramolecular species than nanotubes are formed at different MeOH concentrations of the sample solution, as it was evident from a well-defined isosbestic point around ~530 nm; the same is observed here.

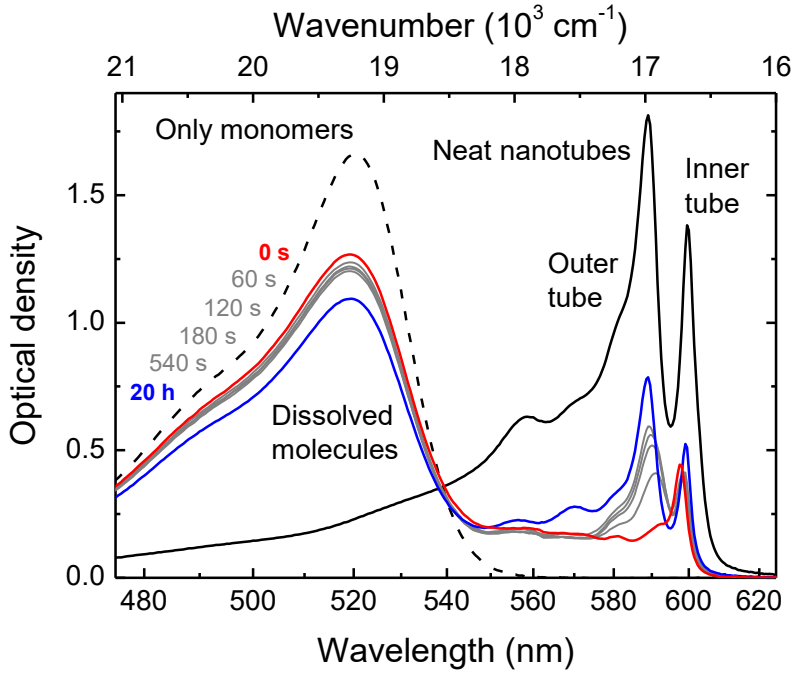

Supplementary Figure 8. Evolution of the absorption spectra and recovery of the outer tube following flash-dilution (red) in a standard cuvette within the first ~9 minutes (gray) and after ~20 hours (blue). The absorption spectra of completely dissolved C8S3 monomers (dashed black) as well as neat double-walled nanotubes (solid black) are shown for comparison. The molar concentration of the sample is $c = 1.11 \times 10^{-4}$ M for all spectra, the thickness of the cuvette is $d = 0.1$ cm.

The balance between the monomer absorption and the optical density of the inner tube peak allows estimating the concentration of molecules that remains embedded in the isolated inner tubes after flash-dilution (c_{inner}), i.e., taking into account the 'loss' of molecules of the outer tube and the complete dissolution of nanotubes. One of the limiting cases is the complete dissolution of nanotubes into monomers (molar concentration $c = 1.11 \times 10^{-4}$ M, extinction coefficient $\epsilon = 1.5 \times 10^{5}$ $\mathrm{M^{-1}\ cm^{-1}}$). In that case one would the following optical density for the monomer peak:

$$\mathrm{OD_{mon}} = \epsilon\, c\, d = 1.66. \qquad (4.1)$$

The corresponding absorption spectrum is shown in Supplementary Figure 8 (dashed line). Meanwhile, right after flash-dilution a peak optical density of only 1.27 at 520 nm is observed

(Supplementary Figure 8, red line). Therefore, one can estimate the fraction of dissolved molecules as

$$\frac{\mathrm{OD_{exp}}}{\mathrm{OD_{mon}}} = \frac{1.27}{1.66} = 77\ \%, \tag{4.2}$$

i.e., 77 % of the maximum number molecules, which corresponds to a concentration of monomers of $c_{\mathrm{mon}} = 8.5 \times 10^{-5}$ M. This, in turn, leaves $c_{\mathrm{inner}} = 2.6 \times 10^{-5}$ M as the concentration of molecules that remained in the inner tube.

As an alternative estimate of c_{inner} one can consider the optical density of the inner tube peak at ~600 nm. In fact, from theoretical models of the nanotubes it is known that ~40 % of the molecules reside in the inner tubes, while the remaining ~60 % reside in the outer tube[2]. In case of perfectly selective dissolution of only the outer tube, while leaving all inner tubes entirely intact, one would expect a concentration of $c_{\mathrm{inner}} = 4.44 \times 10^{-5}$ M. However, in experiment the OD of the inner tube is by factor 3.4 lower than for double-walled nanotubes indicating that ~70 % of the nanotubes were completely dissolved. Hence, one obtains $c_{\mathrm{inner}} = 1.33 \times 10^{-5}$ M, which is in good agreement with the value obtained with the first method. The average value of both concentrations is $c_{\mathrm{inner}} = (2 \pm 0.6) \times 10^{-5}$ M.

5. Post-Flash-Dilution Cryo-TEM

In this section, we investigate the recovery of C8S3 nanotubes following microfluidic flash-dilution by imaging their supramolecular structure using cryogenic transmission electron microscopy (cryo-TEM). Microfluidic flash-dilution was carried out as described in the main text with exception of increased flow-rates (i.e., 3.5 ml h^{-1} diluting agent : 3 ml h^{-1} sample solution) in order to accelerate sample collection. During sample collection the PL spectrum was monitored to ensure stable dissolution of the outer tube. The sample was then transferred to the cryo-TEM sample preparation as fast as possible, but due to logistic reasons the time gap between flash-dilution and freezing was limited to $\sim$15 minutes.

For the actual freezing of the sample we employed the same protocol as described in Ref. [3]. In brief, a 3 µl droplet of the sample solution was placed on a hydrophilized copper grid with holey carbon film (quantifoil 3.5/1). After blotting off excess fluid for 5 s the grid was immediately vitrified in liquid ethane at its freezing point (-184 °C) with a Vitrobot (FEI, Eindhoven, The Netherlands). The grids were placed in a cryotransfer holder (Gatan model 626) and transferred into a Philips CM120 transmission electron microscope with an LaB6 cathode or a tungsten hairpin cathode operated at 120 kV. Micrographs were recorded with an UltraScan 4000 UHS CCD camera (Gatan, Pleasanton, CA, USA) using low-dose mode.

A representative cryo-TEM micrograph of C8S3 nanotubes after flash-dilution is shown in Supplementary Figure 9a. In the sample, we find long nanotubes (length $\gg$ 1 µm), whereas short nanotubes of lengths $<$ 1 µm have not been observed. It is unlikely that the nanotubes grow significantly in length on a timescale of $\sim$15 minutes after flash-dilution, as they are known to self-assemble on a timescale of $\sim$24 hours under normal conditions (i.e., $\sim$11 wt% MeOH)[2]. Here, the MeOH content of the sample solution is $\sim$28 wt%, which likely decelerates the nanotube growth, as the equilibrium point between monomers and nanotubes is shifted towards the former (ESI†, Section 4). Therefore, we conclude that no substantial shortening of the nanotubes occurs during flash-dilution. We will return to the issue of possible nanotube shortening in ESI†, Section 6.

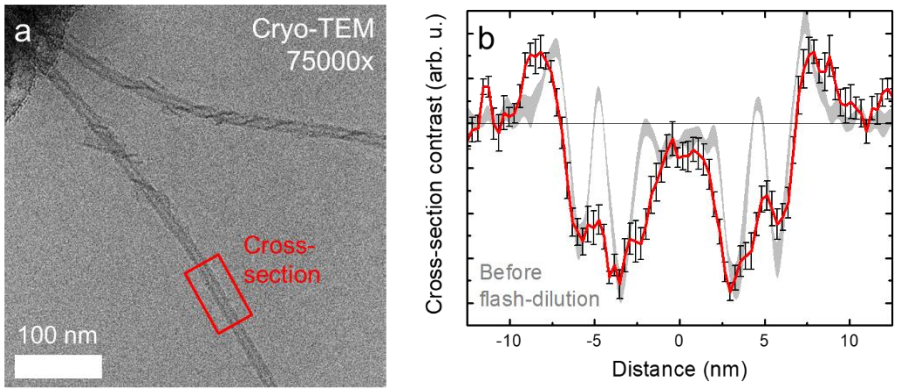

Supplementary Figure 9. (a) High (75000 ×) magnification cryo-TEM micrograph of C8S3 nanotubes ~15 minutes after microfluidic flash-dilution. (b) Cross-sectional profile (red) of the nanotube shown in panel (a). The cross-sectional profile of nanotubes before flash-dilution is shown for comparison (gray).

The cryo-TEM micrograph shows that after flash-dilution the dissolved molecules re-assemble around the exposed inner tubes (in some cases in a helical fashion; Supplementary Figure 9a, upper nanotube) thereby restoring the outer layer, as it was expected based on the linear absorption spectra (ESI†, Section 4). The recovery of the outer layer of the nanotubes is evident from the characteristic modulation of the integrated cross-sectional contrast (Supplementary Figure 9b), where the inner and outer pair of dips corresponds to the inner and outer wall, respectively. We extract the cross-sectional contrast by taking images of straight segments of the same nanotubes (Supplementary Figure 9a; each about 20 nm in length) and integrate those along the long axis of the nanotubes, which yields the integrated contrast profile of this segment. This procedure was repeated for 11 separate segments and subsequently averaged to obtain the cross-sectional cut shown in Supplementary Figure 9b. The total nanotube length over which the contrast was averaged amounts to 220 nm.

In the case of re-assembled nanotubes, the modulation of the cross-sectional profile is clearly visible, which proves the (partial) recovery of the original double-walled structure. This is in line with the recovery of the outer-wall absorption at the timescale of ~10 minutes (Supplementary Figure 8), i.e., approximately when the liquid sample was frozen for cryo-TEM experiments. The modulation depth of the cross-sectional contrast is not as pronounced as for neat nanotubes before flash-dilution (Supplementary Figure 9d, gray; same data as in Ref. [3]). This may either be caused by an increased degree of structural inhomogeneity/disorder of the re-assembled nanotubes or related to the TEM imaging conditions or a combination of both. A similar analysis of shorter

segments with supposedly lower degree of structural inhomogeneities was prevented by the fact that the cross-sectional contrast for each individual segment was too low to accurately identify the boundaries of the inner and outer tube.

To explain the origin and separation of the peaks in the cross-sectional contrast profile it is instructive to consider a simple geometrical model of the nanotubes consisting of two concentric cylinders with thickness h and external radii r_o and r_i (Supplementary Figure 10a). Each cylinder represents the electron density around C8S3 core (see Figure 1c of the main text); the gap between the cylinders account for lower electron density of the hydrophobic tails. The projected amount of material $L(x)$ encountered by electrons (used for TEM imaging) as a function of the spatial coordinate x is shown in Supplementary Figure 10b. In the simplest approximation, the contrast in the TEM image is proportional to the amount of material, as it gives rise to elastic scattering of electrons and phase contrast. We stress, however, that in reality the image formation in a TEM is much more involved and beyond the scope of the considerations presented herein; details can be found in literature[4]. Here, we account for the effects of the finite imaging resolution (depending on the defocus settings, *etc.*) and possible size inhomogeneities along the nanotube axis by convoluting the thickness profile $L(x)$ with a Gaussian function $G(x;\sigma)$ with a standard deviation width σ:

$$L'(x) = L(x) \otimes G(x;\sigma). \qquad (5.1)$$

The thus obtained thickness profiles for nanotubes before and after flash-dilution are shown in Supplementary Figure 10c and d (black), respectively.

The modelled profiles show good agreement of the experimentally obtained profiles (Supplementary Figure 10c and d; gray). In both cases the outer and inner external radii are $r_\mathrm{o} = 6.5$ nm and $r_\mathrm{i} = 4.1$ nm, respectively, and the effective cylinder thickness is $h = 0.6$ nm (i.e., the effective thickness giving rise to most contrast upon TEM imaging). The only difference between the two modelled profiles before and after flash-dilution concerns the convolution according to Eq. 5.1, for which widths of $\sigma = 0$ nm (no convolution) and $\sigma = 0.4$ nm were used. This convolution causes the observed modulation depth of the contrast profile in Supplementary Figure 10d to be less pronounced, although the characteristic sizes of the nanotube remain unchanged. The wall thickness (defined as the difference of the inner and outer tube radii $d = r_\mathrm{o} - r_\mathrm{i}$) amounts to 2.4 nm in both cases.

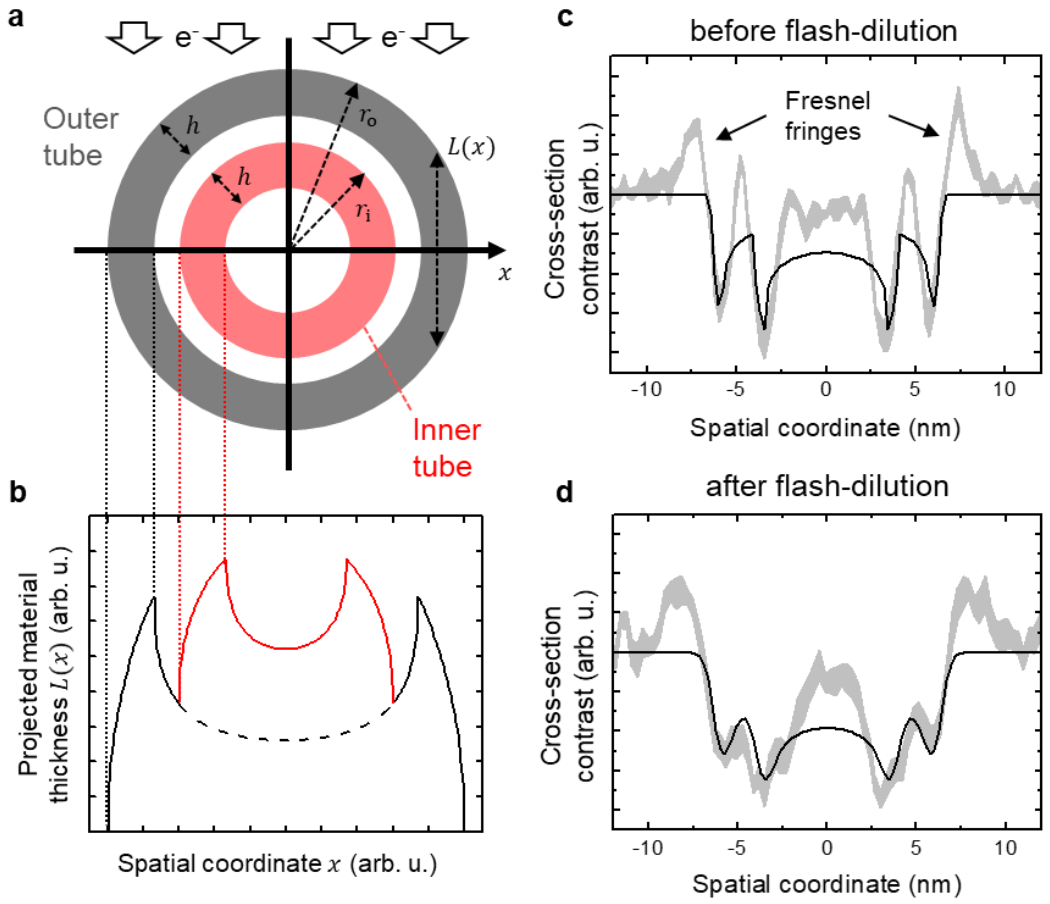

Supplementary Figure 10. (a) Geometrical model of the nanotubes with an outer (gray, external radius r_o) and inner (red, external radius r_i) tube. Each cylinder has an (effective) thickness of h. (b) Projection of the material thickness $L(x)$ of both tubes along the vertical direction as indicated in panel (a). (c, d) Comparison of the experimental cross-sectional profiles (gray) and the profiles $L'(x)$ obtained from Eq. 5.1 before and after flash-dilution. Fresnel fringes as a TEM imaging related artifact are labelled as such in panel (c).

In literature, there exist different metrics concerning the nanotubes' characteristic sizes[2,3,5]. A quantitative comparison would require simulation of the TEM images based on molecular models, as e.g. done in Ref. [6]. Such treatment would substantially improve the agreement of theory and experiment by also taking into account image formation in a TEM (including defocus, *etc.*) as well as other imaging-related effects such as the formation of Fresnel fringes (Supplementary Figure 10c). Nevertheless, with the simple model applied we have shown that the recovered nanotubes can be characterized with the same sizes as the original nanotubes (before flash-dilution).

6. Post-Flash-Dilution Photoluminescence Microscopy

Photoluminescence microscopy experiments were carried out on a home-built setup assembled around a Carl Zeiss Observer D1 microscope. A green CW laser *(*$\lambda = 561$ nm, Coherent Sapphire 561-100) served as illumination source. Next, the circularly polarized excitation beam was split in two separate beams for wide-field and focused excitation. Both beam arms were equipped with mechanical shutters, neutral density filters, and telescope arrangements with a pinhole in their focal positions to expand the beam diameters and spatially filter the intensity distribution. For wide-field excitation an additional lense ($f = 500$ mm) was placed in the beam path. By using a second beamsplitter both beams were collinearly coupled into the microscope, which contained a filter cube with a longpass dichroic mirror and bandpass filter ($575 - 640$ nm, Carl Zeiss). An objective (NA $= 0.26$, $10\times$ magnification, Melles Griot) focused the excitation light onto the sample and subsequently collected the PL. The latter was then either imaged directly using a microscope camera (Photometrics Coolsnap HQ2) and an image magnifier ($1.6\times$) or fooorrr spectral acquisition coupled into multi-mode optical fiber connected to a spectrometer (spectral resolution 12 cm^{-1}) equipped with an EMCCD camera (PhotonMax 512, Princeton Instruments).

In order to ensure that no substantial shortening of the nanotubes occurs upon microfluidic flash-dilution, we use photoluminescence (PL) microscopy to directly image the nanotubes. For microscopy, nanotubes were immobilized on glass cover substrates using a drop-flow technique (as e.g. described in Refs. [7,8]). First, microscope glass cover slips (22×22 mm, thickness $\sim$170 µm) were cleaned by submerging them in a 1: 1: 2 ratio of H_2O_2/NH_4OH/H_2O solution for 24 hours. Prior to sample deposition the substrates were rinsed with pure methanol and dried with compressed air. Next, a droplet ($5 - 10$ µl) of neat or flash-diluted nanotube sample solution was applied to the top edge of the glass cover that was inclined by $30° - 45°$ relative to the lab bench. The droplet quickly rolled off the inclined glass cover substrate leaving a thin film on the surface. In the case of flash-dilution, a droplet of the sample solution was directly applied from the output of the microfluidic flow-cell in order to minimize the time gap between microfluidic flash-dilution and sample deposition. The samples were kept in a black box for $\sim$1 hour for drying, and subsequently transferred to the microscope.

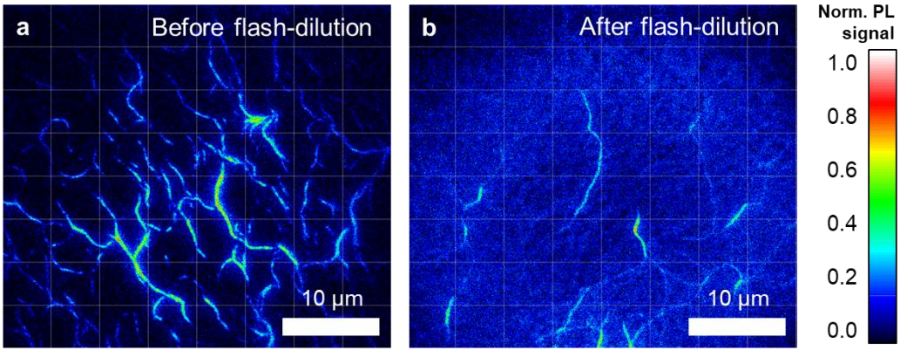

Supplementary Figure 11. Wide-field excitation images of C8S3 nanotubes deposited on a cover glass (a) before and (b) after microfluidic flash-dilution. The PL intensity was normalized to the maximum amplitude in the image and is depicted on a linear color scale between 0 and 1.

A direct comparison of wide-field excitation microscopy images recorded before flash-dilution (i.e., neat double-walled nanotubes) and directly after microfluidic flash-dilution is shown in Supplementary Figure 11a and b. The image of neat C8S3 nanotubes shows a dense, fibrous network with nanotube lengths ranging from few µm's up to tens of µm's; consistent with previous studies[7,8]. After flash-dilution, the nanotube network is less dense and shows a more pronounced background. The background quickly photobleaches, which is the reason for the donut shaped intensity pattern in Supplementary Figure 11b, where the background in the center has bleached most due to the highest light intensity. We ascribe the increased background to single molecules that were dissolved during microfluidic flash-dilution. Upon immobilization of the sample on a substrate, these dissolved molecules form a thin, continuous film, which bleaches easily under ambient conditions. Taken together with the reduced density of nanotubes, this also indicates the complete dissolution of nanotubes upon flash-dilution.

Comparing the images before and after flash-dilution, no substantial changes of the nanotube lengths are found, i.e., in both cases nanotube lengths are on the order of a few µm's up to tens of µm's). We stress that although changes of the molecular structure upon immobilization and drying may potentially occur, considerable growth of the nanotubes' length is very unlikely given the short time gap between flash-dilution and sample deposition and the low molar concentration of the sample. Therefore, we refrain from inferring any further conclusion regarding the structure-spectroscopic properties of the nanotubes, but can safely conclude that flash-dilution does not lead to (systematic) shortening of the nanotubes' lengths (down to sub-100 nm length, where the nanoconfinment effects are expected to occur[9]).

7. Estimation of the Exciton Density

The exciton density, i.e., the number of excitons (N_e) normalized by the number of molecules (N_m) in the focal volume, was calculated as follows (as for example done in Ref. [10]):

$$\frac{N_\mathrm{e}}{N_\mathrm{m}} = \frac{P}{f\ h\ c_0}\left(\frac{1}{\pi\ r_\mathrm{focal}^2}\right)\left(\frac{\int I_\mathrm{exc}(\lambda)\ \lambda\left(1-10^{-A(\lambda)}\right)d\lambda}{\int I_\mathrm{exc}(\lambda)d\lambda}\right)\left(\frac{1}{U c N_A d}\right). \tag{7.1}$$

Here, P is the average excitation power, f is the repetition rate of the laser pulses, h is Planck constant and c_0 the speed of light. The first bracketed term computes the excitation spot area across which the intensity distribution is assumed flat (ESI†, Section 2). The second bracketed factor accounts for the spectral overlap of the sample absorption spectrum ($A(\lambda)$) and the excitation laser spectrum ($I_\mathrm{exc}(\lambda)$). The number of molecules per unit area is then calculated in the third bracketed factor as the product of the Avogadro constant N_A, the molar concentration of the sample c and the thickness d of the focal volume (as determined by the thickness of the microfluidic channel $50\ \mu\mathrm{m}$). U is a correction factor, which rescales the effective number of molecules in flash-dilution experiments, i.e., the number of molecules that remain embedded in the inner tubes (ESI†, Section 4). The origin of this scaling factor is two-fold: first, the outer layer is physically dissolved thereby removing molecules from the spectral window that is probed in the experiment. Secondly, flash-dilution also leads to the partial dissolution of inner tubes, which manifests itself as an overall reduction of the optical density compared to neat nanotube solution. For the combined effect, i.e., flash-dilution and partial dissolution, we find $U = U_{FD}\ U_{CD} \approx 0.175$ by comparing the (effective) molar concentration before and after flash-dilution. In the case of double-walled nanotubes $U = 1$. The error of the exciton density was calculated as the propagation of uncertainty from all experimental inputs.

8. Photoluminescence Decay Maps

A set of representative PL decay maps of double-walled nanotubes and isolated inner tubes is shown in Supplementary Figure 12a and b, respectively. Gradually increasing the exciton density (from left to right) leads to a progressive acceleration of the PL decay (vertical axis), while the PL spectra remain unchanged (horizontal axis). The PL decay maps are superimposed with the respective PL mean frequency ($\langle \nu(t) \rangle$; white lines) that shows that no spectral relaxation occurs on the timescale of emission, i.e., within the experimental uncertainty the PL mean frequency is a vertical line in Supplementary Figure 12.

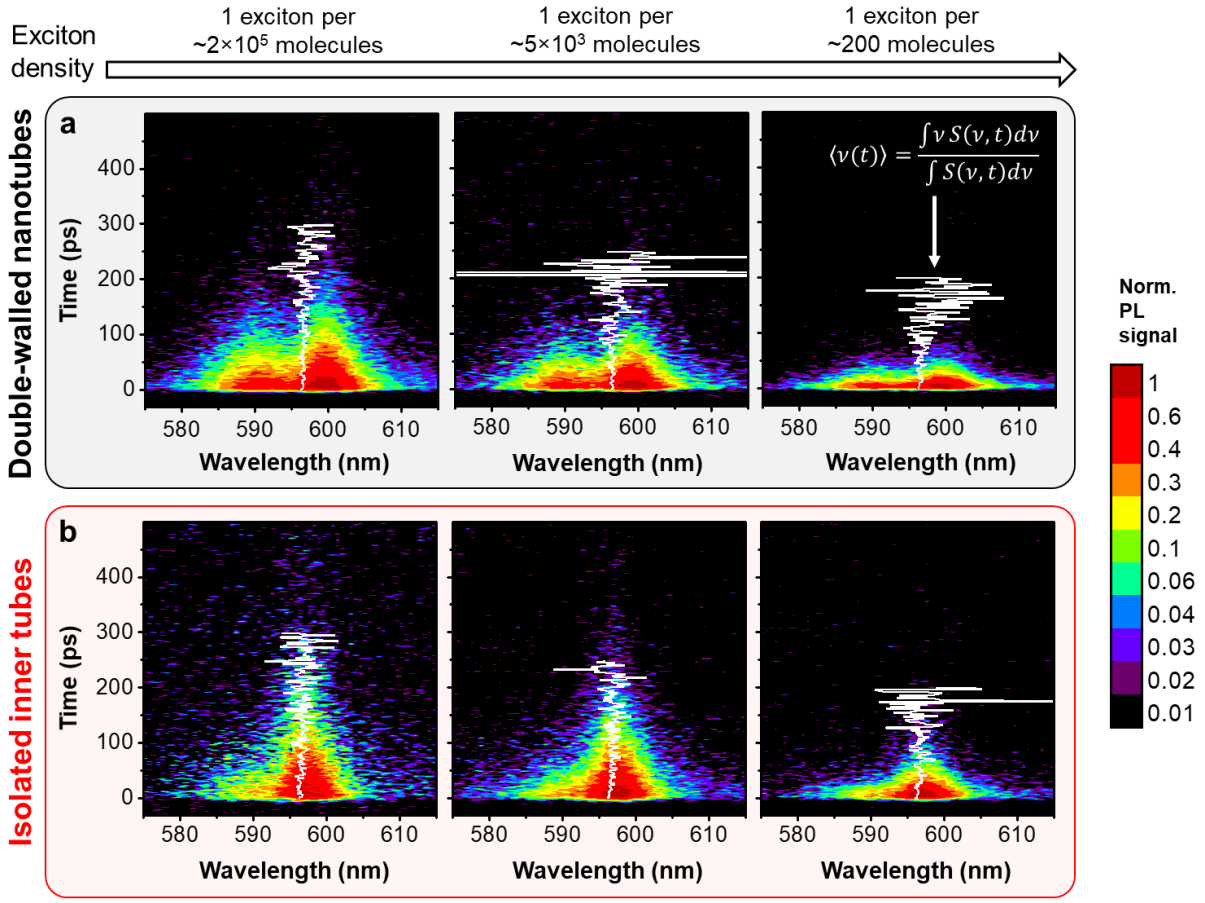

Supplementary Figure 12. Representative PL decay maps for (a) double-walled nanotubes (shaded in gray) and (b) isolated inner tubes (shaded in red) at different exciton densities (increasing from left to right). The PL amplitudes were normalized to the respective maximum value and are depicted on a logarithmic color scale between 0.01 and 1. The mean frequency (or first moment) of the PL spectra $\langle \nu(t) \rangle$ as a function of time is shown as a white line superimposed with the PL decay maps. The formula for the calculation of $\langle \nu(t) \rangle$ with $\nu = \lambda^{-1}$ is given in the inset.

Supplementary Figure 13 depicts the maximum PL amplitude extracted from the experimental PL transients as a function of exciton density. The difference in PL amplitude (by factor ~6) of double-walled nanotubes and isolated inner tubes is caused by the lower molar concentration in the latter case due to removal of the outer tube as well as complete dissolution of nanotubes (ESI†, Section 4). In absence of EEA, the PL amplitudes are proportional to the exciton density and, thus, scale linearly as a function of the latter. Deviations from this behaviour, therefore, indicate non-radiative loss of excitons due to EEA occurring faster than the streak camera permits to resolve. Solid lines are obtained from MC simulation of the exciton dynamics and reflect the same trend observed in experiment; the amplitudes of the simulations were scaled to match the experimental PL amplitude.

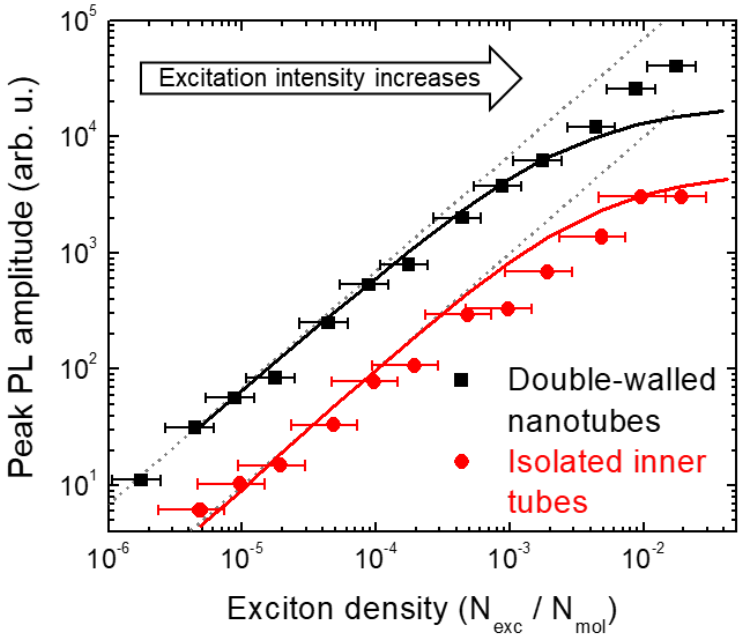

Supplementary Figure 13. Log-log plot of the maximum PL amplitude of double-walled nanotubes (black dots) and isolated inner tube (red dots) as a function of exciton density. Reference lines (gray dotted) are drawn for a linear dependence of the PL amplitude *versus* exciton density, i.e., the slope of 1 in the log-log plot. The horizontal error bars (for the exciton density) are obtained from propagation of uncertainty of all input parameters (ESI†, Section 7). Solid lines are derived from Monte-Carlo simulations.

9. Control Experiments on Dissolved C8S3 Molecules

In this section, we verify that the observed acceleration effects of the PL dynamics are correctly ascribed to exciton-exciton annihilation (EEA) and do not arise from other non-linear effects of the individual molecules. Therefore, we conduct control experiments on diluted C8S3 molecules in the same setting as for isolated inner tubes and double-walled nanotubes. In solution, the individual molecules are well separated (average intermolecular distance ~ 20 nm for the given concentration; *vide infra*) and, thus, non-interacting. This prevents the formation of excitons as collective excited states and, thus, also prevents EEA.

For the experiments, the same setup as described in the methods section of the main text was used. Here, the tear-drop mixing flow-cell was used to mix concentrated C8S3 stock solution (molar concentration $c = 1.75 \times 10^{-3}$ M) with pure methanol (MeOH) at a $1:9$ ratio rendering a final dye concentration of $c = 1.75 \times 10^{-4}$ M. In comparison, the molar concentration of regular sample solution after flash-dilution is $c = 1.11 \times 10^{-4}$ M. Taken together with the extinction coefficient of C8S3-Cl in MeOH ($\epsilon = 1.5 \times 10^{8}$ cm^2 mol^{-1}) and a channel thickness of 50 µm this gives rise to a maximum optical density on the order to ~ 0.1. The excitation wavelength was chosen as 530 nm (Supplementary Figure 14a; green). Due to the dichroic mirror in the experimental setup, the monomer PL spectrum was truncated at ~ 565 nm and only the tail could be analyzed (Supplementary Figure 14a); as was the case in ESI†, Section 3. The integrated PL transients of dissolved C8S3 molecules at different excitation powers are shown in Supplementary Figure 14b.

Supplementary Figure 14c shows that the PL decay rate of dissolved C8S3 molecules remains unchanged across the entire range of optical excitation powers proving that no neither EEA nor any other unwanted non-linear effects occur. Fitting the transient to a convolution of an exponential decay and a Gaussian function (as an approximation of the instrument response function) yields PL lifetimes of 97 ± 21 ps (low intensity), 116 ± 14 ps (medium intensity), and 115 ± 7 ps (high intensity). The error margins refer to the standard deviation of the respective fit. For all three measurements combined, one finds an average PL lifetime of 109 ± 6 ps, where the error margin is the standard error of the mean.

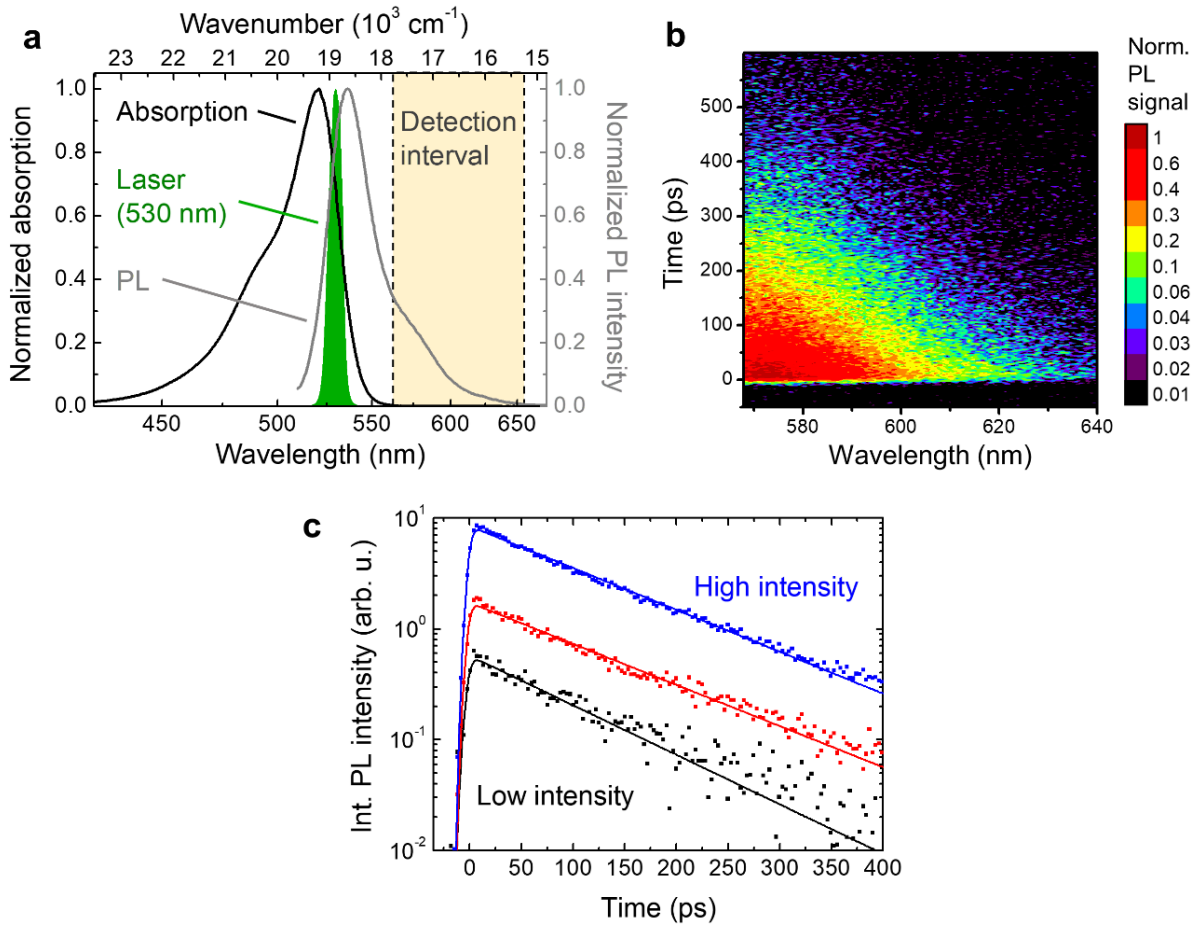

Supplementary Figure 14. (a) Normalized absorption (black) and PL (gray) spectra ($\lambda_{exc} = 500$ nm) of C8S3 monomers dissolved in MeOH. The laser excitation spectrum at 530 nm used for time-resolved PL measurements is shown in comparison (green). Shaded region: Detection interval accessible in streak camera measurements due the use of a dichroic mirror and additional spectral filters that block the excitation light. (b) Representative PL decay map of C8S3-Cl monomers in MeOH recorded for the highest excitation intensity in experiment resulting in 1 excitation per ~60 molecules. The PL amplitude was normalized to the maximum value and is depicted on a logarithmic color scale between 0.01 and 1. (c) Spectrally integrated PL transients at excitation densities of 1 excitation per ~6000 molecules (black dots), ~600 molecules (red dots) and ~60 molecules (blue dots); ESI†, Section 7. Fits of the experimental data with a convolution of an exponential decay and a Gaussian function (representative for the instrument response function) are shown as solid lines in the corresponding colors.

10. Monte-Carlo Simulations

A complete overview of model parameters for MC simulations is given in Supplementary Table 1; details on the construction of the molecular grid can found in Ref. [11]. The initial exciton density induced by the laser pulse was set according to Eq. 7.1 in ESI†, Section 7.

Supplementary Table 1. Overview of parameters in MC simulations.

Parameter	**Symbol**	**Isolated inner tubes**	**Double-walled nanotubes**	**Source**
Hopping rate (fs^{-1})	H	0.04	0.04	Same as in Ref. [11]
Annihilation radius (# of molecules)	$R_{\mathrm{ann}}^{\mathrm{inner}}$ $R_{\mathrm{ann}}^{\mathrm{outer}}$	3 –	3 3	Same as in Ref. [11]
Molecular grid size Inner layer Outer layer		30×10000 –	30×10000 55×10000	(Width × length) Derived from theoretical model of nanotubes in Ref. [2]
Lifetime (ps)	τ	58	43	PL transients at low exciton densities (1 exciton per $\sim 10^5$ molecules)
Exciton transfer rate (fs^{-1}) Outer → inner Inner → outer	 k_{oi} k_{io}	 – –	 0.0031 0.0013	2D spectroscopy; same as in Ref. [11]
Simulation step size (fs)	Δt	1	1	Same as in Ref. [11]
Saturation trap density	n_{sat}	10^{-4}	10^{-4}	Fitting parameter

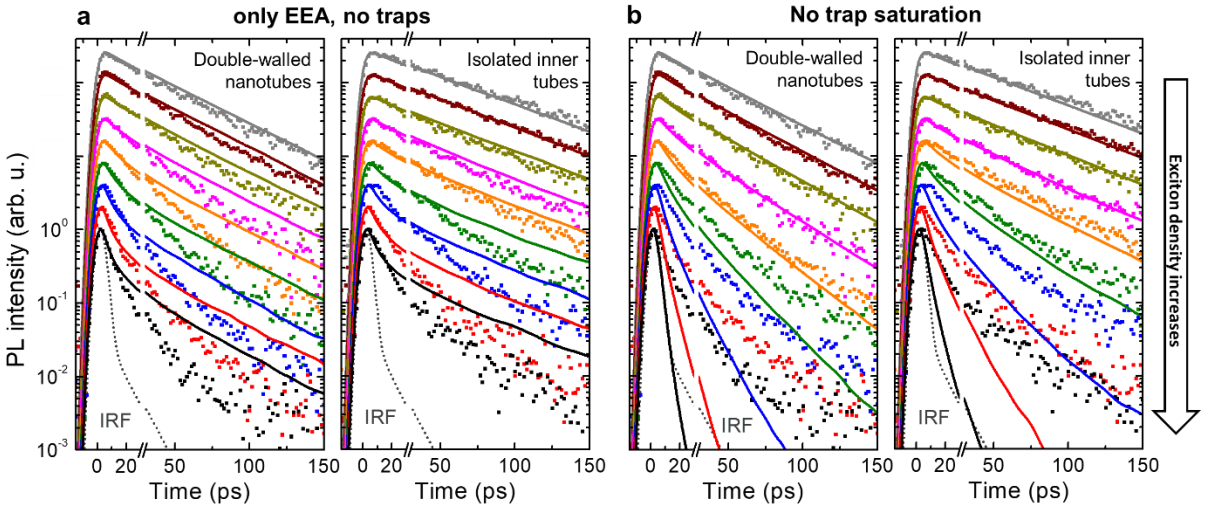

Supplementary Figure 15. Logarithmic plots of the experimental PL transients (dots) for double-walled nanotubes and isolated inner tubes recorded at different exciton densities (increasing from top to bottom); the experimental data are identical to Figure 4 in the main text. Results from MC simulations are shown as solid lines in the respective color for (a) simulations of the exciton dynamics including EEA, but excluding the formation of traps and (b) including both EEA and the formation of traps, but neglecting the saturation trap density (n_{sat}).

Supplementary Figure 15a shows the PL transients for double-walled nanotubes and isolated inner tubes obtained from MC simulations (solid lines), in which excitons can only decay naturally or undergo EEA. The simulated transients show good agreement with the experimental data in the first interval, i.e., the initial 30 ps of the PL decay that are governed by EEA. During that time most of the excitons have either already undergone EEA or decayed naturally so that the total number of excitons is strongly depleted, which inhibits further EEA. Consequently, the simulated PL signal decays with the intrinsic (non-)radiative lifetime at longer times, which strongly overestimates the PL amplitude in the tail observed in experiment.

Supplementary Figure 15b shows the simulated PL transients (solid lines), where excitons formed traps upon decay (naturally or via EEA), but the saturation trap density (n_{sat}) was not included (no saturation allowed). At low exciton densities the simulations agree well with the experimental data (dots), whereas at high exciton densities the trap induced acceleration strongly overestimates the experimentally observed trends; this is also reflected in the PL decay rates in Figure 5a and b in the main text. In order to globally fit all transients (double-walled nanotubes as

well as isolated inner tubes) we therefore had to include the saturation trap density in the MC simulations.

11. EEA PL Dynamics at Different Flow Velocities

In this section, we investigate whether photo-induced effects such as (accumulated) bleaching of the nanotubes or other detrimental effects play a role for the observed PL dynamics. Due to the high repetition rate of the laser (80 MHz) and the relatively low flow speed in the microfluidic cuvette ($\sim$6 mm s^{-1}), one may suspect that the exposure of the same sample in the focal volume to a large number of laser pulses leads to accumulation effects such as a progressing degradation of the nanotubes or a rising temperature. In order to rule out any accumulation effects, we performed the same experiments using a conventional flow cuvette (Hellma, optical pathlength 50 µm) and a peristaltic pump (Masterflex) that is able to provide higher flow speeds and compared the results to the case of microfluidics. Based on the flow velocities we estimate the average number of pulses the nanotubes are exposed to in the focal volume during a typical measurement before being refreshed with new sample solution. This is summarized in Supplementary Table 2.

Supplementary Table 2. Estimate of the average number of laser pulses that nanotubes in the focal volume are exposed to during a typical measurement.

	Symbol	**Microfluidics**	**Ordinary flow cuvette**
Flow rate	F	600 µl h^{-1} 1.67×10^{-4} ml s^{-1} 0.167 mm^3 s^{-1}	- 0.64 ml s^{-1} 640 mm^3 s^{-1}
Channel cross section	A	0.025 mm^2	0.45 mm^2
Flow velocity	v_{flow}	$\sim$6.7 mm s^{-1}	$\sim$1422 mm s^{-1}
Laser repetition rate	f_{laser}	80 MHz $= 8 \times 10^7 s^{-1}$	
Focal volume diameter	d_{foc}	3.2 µm $= 3.2 \times 10^{-3}$ mm	
Avg. number laser pulses	N_{pulses}	$\sim$40000	$\sim$200
Ratio	R	$\frac{40000}{200} = 200$	

We find that in microfluidic experiments the same focal volume accumulates $\sim$40000 pulses, whereas for circulative pumping this number is significantly reduced down to $\sim$200 pulses. Despite this lower number of accumulated pulses, the transients are found identical

(Supplementary Figure 16), which implies that accumulation effects do not play a role. In other words, the observed acceleration of the PL dynamics is caused by each pulse (or a very small number of pulses) and not a measurement related artefact due to exposure to a large number of laser pulses.

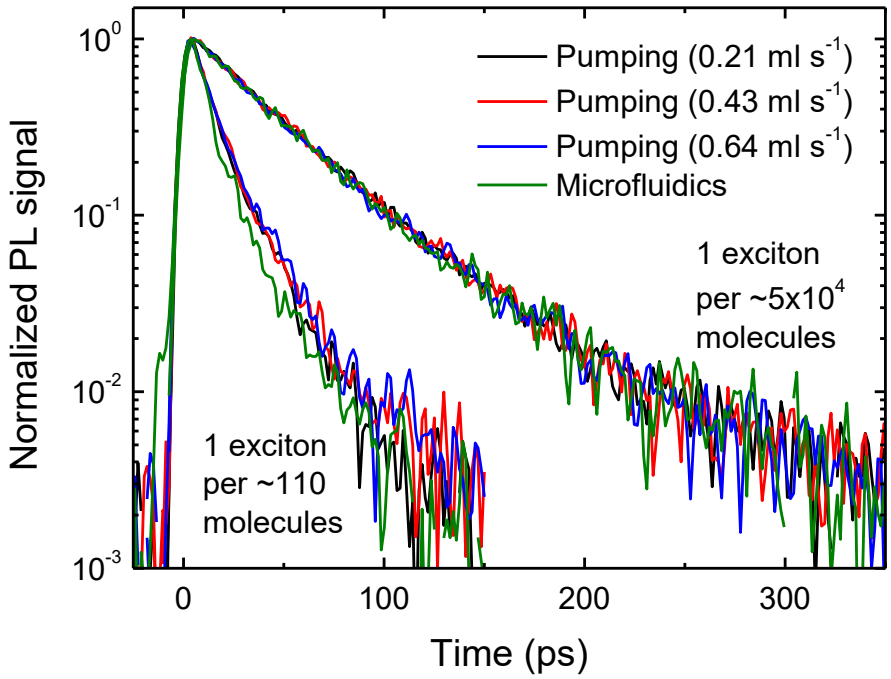

Supplementary Figure 16. Normalized PL transients from EEA PL experiments employing a conventional flow cuvette (black, red, blue) and a microfluidic flowcell (green) at high and low exciton densities of 1 exciton per ~110 and ~5×10^4 molecules, respectively. The high exciton density transients were cropped at 150 ps.

The small difference between the PL transients from microfluidics experiments (Supplementary Figure 16; green) and circulative pumping (Supplementary Figure 16; red, blue, and black) at high exciton densities may arise from a mismatch of the exciton density in the two experiments. Using a conventional flow cuvette instead of a microfluidic flow-cell may have slightly affected the focusing conditions of the excitation light into the cuvette. In the EEA regime, already small changes of the spot size have profound impact on the exciton density and, thus, on the observed acceleration of the PL dynamics. At low exciton densities, this is not an issue, as the PL transients are solely determined by the (non-)radiative lifetimes. Small deviations in the exciton density do not immediately lead to an acceleration of the PL decay.

12. Photoluminescence Dynamics at Different Temperatures

In this section, we investigate possible effects of an increased temperature on the PL lifetime of double-walled nanotubes. The relevance of this is that the excess energy released by exciton-exciton annihilation (locally) heats up the sample before it is dissipated into the bulk solvent. This local raise in temperature (considered in detail in Ref. [11]) may potentially affect the observed PL dynamics.

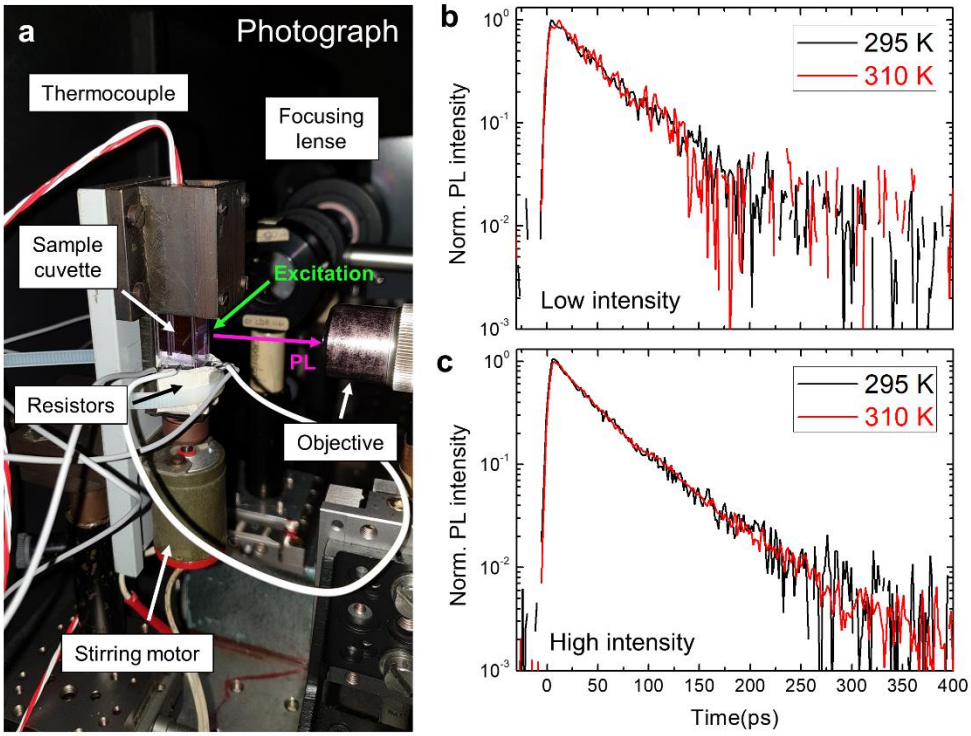

Supplementary Figure 17. (a) Photograph of the experimental setup for temperature dependent time-resolved PL measurements with all essential elements labelled. The directions of the excitation beam (green) and the PL signal (magenta) are shown with colored arrows. (b, c) Integrated PL transients of C8S3 nanotubes at room temperature (295 K, black line) and higher temperature (310 K, red line) recorded under (b) low excitation intensity and (c) high excitation intensity.

Temperature control of the sample solution (molar concentration $c \approx 3.34 \times 10^{-6}$ M) was realized in a standard 10 mm quartz cuvette (Starna, Germany) from which the PL signal was collected in a 90° geometry (with respect to the excitation beam); a photograph of the experimental arrangement is shown in Supplementary Figure 17a. The sample solution was heated by using two resistors in thermal contact with the exterior of the cuvette. During the experiment, the sample was

continuously stirred using a magnetic stirring bar and its temperature was monitored by a thermocouple. The excitation light ($\lambda_{\mathrm{exc}} = 550$ nm) was focused by a $f = 7$ cm lense. Using neutral density filters the average excitation power was set to 600 nW or 30 µW.

Supplementary Figure 17b and c show PL transients of double-walled nanotubes recorded at room temperature (295 K, 22°C; red) and at an increased temperature (~310 K, ~37°C; black) at low and high excitation intensities, respectively. In both cases, the PL transients at the two different temperatures are identical. Hence, the PL decay is insensitive to (mild) changes of the temperature, which therefore do not have to be considered in explaining the observed changes of the PL dynamics. Under the focusing conditions in these experiments the exciton-exciton annihilation regime cannot be reached at the given excitation intensities.

13. References

1 H. von Berlepsch, S. Kirstein, R. Hania, A. Pugžlys and C. Böttcher, *J. Phys. Chem. B*, 2007, **111**, 1701–1711.

2 D. M. Eisele, C. W. Cone, E. A. Bloemsma, S. M. Vlaming, C. G. F. van der Kwaak, R. J. Silbey, M. G. Bawendi, J. Knoester, J. P. Rabe and D. A. Vanden Bout, *Nat. Chem.*, 2012, **4**, 655–662.

3 B. Kriete, A. S. Bondarenko, V. R. Jumde, L. E. Franken, A. J. Minnaard, T. L. C. Jansen, J. Knoester and M. S. Pshenichnikov, *J. Phys. Chem. Lett.*, 2017, **8**, 2895–2901.

4 L. Reimer and H. Kohl, *Transmission Electron Microscopy*, Springer, 2008.

5 Y. Qiao, F. Polzer, H. Kirmse, E. Steeg, S. Kirstein and J. P. Rabe, *J. Mater. Chem. C*, 2014, **2**, 9141–9148.

6 C. Friedl, T. Renger, H. von Berlepsch, K. Ludwig, M. Schmidt am Busch and J. Megow, *J. Phys. Chem. C*, 2016, **120**, 19416–19433.

7 D. M. Eisele, J. Knoester, S. Kirstein, J. P. Rabe and D. A. Vanden Bout, *Nat. Nanotechnol.*, 2009, **4**, 658–663.

8 K. A. Clark, E. L. Krueger and D. A. Vanden Bout, *J. Phys. Chem. Lett.*, 2014, **5**, 2274–2282.

9 A. Bondarenko, PhD Thesis, University of Groningen, 2019.

10 J. Dostál, F. Fennel, F. Koch, S. Herbst, F. Würthner and T. Brixner, *Nat. Commun.*, 2018, **9**, 2466.

11 B. Kriete, J. Lüttig, T. Kunsel, P. Malý, T. L. C. Jansen, J. Knoester, T. Brixner and M. S. Pshenichnikov, *Nat. Commun.*, 2019, **10**, 4615.